Luminescence measurements of hyperthermal $Xe^{2+} + O_2$ and $O^+ + Xe$ collision systems

SCHOLARONE™
Manuscripts

Luminescence measurements of hyperthermal Xe²⁺ + O₂ and O⁺ + Xe collision systems

Michael L. Hause[1], Sierra Solter[1], Benjamin D. Prince[2] and Raymond J. Bemish[2]

[1]Institute for Scientific Research, Boston College, Chestnut Hill, Massachusetts 02159, USA

[2]Air Force Research Laboratory, Space Vehicles Directorate, Kirtland AFB, NM 87117, USA

Abstract

Emission excitation cross sections are recorded for collisions between $Xe^{2+} + O_2$ and $O^+ + Xe$ over a collision energy range of approximately 2 to 900 eV in the center-of-mass (E_{cm}) frame. Emissive products of the $O^+ + Xe$ reaction are examined in the 700-1000 nm optical range and include neutral atomic oxygen emissions and neutral xenon emissions. Atomic emission products of the $O^+ + Xe$ collision appear to have measureable cross sections near $E_{cm} = 14$ eV and increase in intensity until about $E_{cm} = 60$ eV where they remain approximately constant for the remainder of the measured collision energies. For the $Xe^{2+} + O_2$ collision system, O_2^+ charge transfer products are measured through fluorescence of the O_2^+ (*A-X*) and (*b-a*) manifolds over the 200-850 nm window. Total cross sections for both manifolds do not vary beyond the experimental precision at all measured energies. Vibrational populations are derived from a fitting of the experimental data. The populations are found to deviate from a Franck-Condon distribution at all collision energies and appear to be well-modeled within a multi-channel Landau-Zener framework over the collision energy range measured.

Introduction

Hyperthermal reactions of $O^+ + Xe$ and $Xe^{2+} + O_2$ are important processes in the local environment of spacecraft using xenon-based electric propulsion systems in low Earth orbit (LEO). These devices create and accelerate Xe^+ and Xe^{2+} ions to kinetic energies ranging from 100 eV/q to 2000 eV/q. In LEO, the emitted ions and neutrals in the plume of the thruster can interact directly with the most abundant atmospheric species such as N_2, O_2, O (>10^9 atoms/cm³ at 200 km altitude)
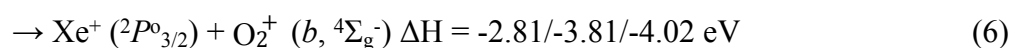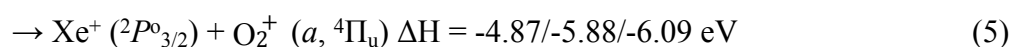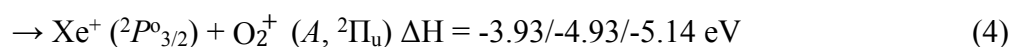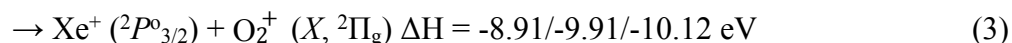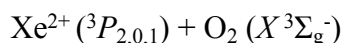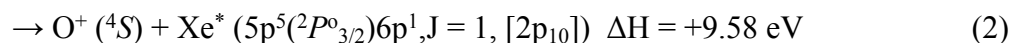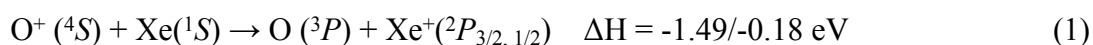
and ionospheric O^+ through high kinetic energy collisions and charge-exchange processes.[1-3] At 8 km/s (a typical speed of a satellite in LEO) the flux of atmospheric species can reach values of $\sim 10^{17}$ atoms/s and, depending on the velocity of the plume constituent, collisions can occur with energies ranging from a few to hundreds of eV in the center-of-mass frame. High energy collisions are expected to result in electronic excitation that likely lead to optical emissions in atomic and diatomic species. In addition, it is anticipated that charged products such as O_2^+, Xe^+ and O^+ can be expected from the normal operation of these electric propulsion systems in a sufficiently dense atmosphere.

Beyond electric propulsion systems, the study of ion-atom/molecule reactions over a wide collision energy range provides insights into gas phase reaction dynamics, charge-transfer mechanisms, non-adiabatic processes and the importance of ion/molecule interaction periods in determining the product rovibrational states. For a specific, related example, Bastian et al. examined the energy dependence of the O^+ (^4S) + Xe charge-transfer collision over a center-of-mass (E_{cm}) collision energy range of 0.1 to 35.2 eV. They found the charge-exchange cross section to increase monotonically over this range with values of 0.72 $Å^2$ (at 0.1 eV) to 26.9 $Å^2$. The dominant charge-exchange product resulted from a Demkov-type direct electron exchange at long range while a minor product, <3 $Å^2$ at the highest collision energies, was ascribed to lower impact parameters involving a Landau-Zener-type curve-crossing mechanism.[4] In studies examining long-range charge exchange with vibrational state resolution, when interaction times are longer than the molecular vibrational period, the resulting product molecular vibrational states can deviate significantly from distributions found in photoionization or electron impact studies (Franck-Condon distributions).[5-12]

Turning to doubly-charged ions and neutral collision partners, efficient single electron transfer is generally linked to the reaction window mechanism.[9, 13-16] In this qualitative description,

charge-transfer is efficient when the long-range attractive reactant polarization potential and repulsive product Coulomb potential cross at interatomic distances between 3-6 Å. This is typically true of those charge transfer reactions that are exothermic by 2-5 eV.

In this work, we examine the luminescence resulting from collisions of firstly $O^+ + Xe$ and secondly $Xe^{2+} + O_2$ in the 250-1000 nm optical regime over a wide collision energy range. Particular emphasis is given in the first reaction to excitation of the electronic states of neutral xenon which emit in the near infrared and thus may impact previously developed collisional radiative models.[17] In the second reaction, particular emphasis is placed on the excited O_2^+ electronic states that are predicted by the reaction window mechanism and previously described theories. The relevant energetics for vibrational ground states of the reactions are:

$$O^+ \, (^4S) + Xe(^1S) \rightarrow O \, (^3P) + Xe^+(^2P_{3/2, \, 1/2}) \quad \Delta H = \text{-1.49/-0.18 eV} \tag{1}$$

$$\rightarrow O^+ \, (^4S) + Xe^* \, (5p^5(^2P^o_{3/2})6p^1, J = 1, [2p_{10}]) \quad \Delta H = \text{+9.58 eV} \tag{2}$$

$$Xe^{2+} \, (^3P_{2,0,1}) + O_2 \, (X \, ^3\Sigma_g^-)$$

$$\rightarrow Xe^+ \, (^2P^o_{3/2}) + O_2^+ \, (X, \, ^2\Pi_g) \, \Delta H = \text{-8.91/-9.91/-10.12 eV} \tag{3}$$

$$\rightarrow Xe^+ \, (^2P^o_{3/2}) + O_2^+ \, (A, \, ^2\Pi_u) \, \Delta H = \text{-3.93/-4.93/-5.14 eV} \tag{4}$$

$$\rightarrow Xe^+ \, (^2P^o_{3/2}) + O_2^+ \, (a, \, ^4\Pi_u) \, \Delta H = \text{-4.87/-5.88/-6.09 eV} \tag{5}$$

$$\rightarrow Xe^+ \, (^2P^o_{3/2}) + O_2^+ \, (b, \, ^4\Sigma_g^-) \, \Delta H = \text{-2.81/-3.81/-4.02 eV} \tag{6}$$

Charge exchange from O^+ to Xe, as shown in reaction 1 with both species in their lowest electronic ground states, is exothermic for both spin-orbit Xe^+ products. Jullien et al. measured the electric dipole forbidden transition $Xe^+ \, (^2P_{1/2} \rightarrow \, ^2P_{3/2})$ and found a radiative lifetime of 49 ms.[18] This lifetime is sufficiently long that essentially none of the radiance is expected to be captured in this experiment. For reaction 2, the non-reactive collision of O^+ and Xe, requires at least 9.58 eV to generate detectable emissions in the near-infrared. Reactions (3)-(6), all charge exchange

reactions between Xe^{2+} and O_2, are exothermic. In these equations, the three enthalpy values listed

reflect the Xe^{2+} in its possible $^3P_2$, $^3P_0$, and $^3P_1$ spin-orbit states ordered in increasing energy. For

the $Xe^+(^2P^o_{3/2})$ product ion, the exothermic range is about 3 to 10 eV for the vibrational ground

states of the various electronic states of product O_2^+. From the same reactants, the Xe^+ $(^2P^o_{1/2})$

product ion is less exothermic by 1.306 eV. Additional electronic states of Xe^{2+}, (^1D and ^1S), with

energies ~2.12 and ~4.48 eV above Xe^{2+} ($^3P_2$), respectively, may also contribute to charge-transfer

products, but whose energetics are not directly shown above. In some cases, the excess reaction

enthalpy may produce significant vibrational excitation of the O_2^+ product ion, possibly over 20

quanta in the A state.

Two of the O_2^+ electronic excited states likely produced, namely the O_2^+ (A) and (b) states,

are known to radiate with high efficiency to the X $(^2\Pi_g)$ and a $(^4\Pi_u)$ electronic states,

respectively.[19] The O_2^+ $(A\text{-}X)$ emission band occurs generally in the range of 200-500 nm while

the O_2^+ $(b\text{-}a)$ emission band occurs in the 450-900 nm range. Direct measurement of the energy

dependence of the emissions from both bands enables examination of the change in state-to-state

charge transfer dynamics as a result of the ion/neutral interaction time.

While the reaction window mechanism prediction of expected vibrational states is

qualitatively illustrative, energy dependent measurements of the vibrational populations provide

an opportunity to examine semi-quantitative predictive techniques such as Landau-Zener and

Demkov approaches to single electron transfer.[20, 21] In both approaches, the electronic coupling,

H_{12}, is critical for the estimation of electron hopping probability between diabatic states. Olson et

al. correlated ninety-nine calculated and measured values to arrive at a semi-empirical prediction

for the H_{12} values generated from simple physical properties, such as the effective ionization

potential of the reactant and products. The H_{12} values were generally accurate to within a factor

of 3 for atomic ion-atom systems.[22, 23] The general form of this coupling is given as:

$$H_{12}^* = AR^* \exp(-BR^*) \tag{7}$$

where A and B are constants and R^* is the interfragment distance. The empirical eqn. 7 must be

converted to system specific values using physical constants of the ion and target, described later

and in ref. 22 and 23. Extension beyond atomic ion-atom collision systems has also found

reasonable agreement to this functional form. Archirel and Levy examined the ArN_2^+ system

where the electronic coupling was calculated through the use of quantum mechanical calculations

and found the A and B term accurate to within a factor of ~4.2 and ~1.4, respectively, for the

ground electronic state-ground vibrational state potentials.[24] They found the coupling for excited

electronic states was sufficiently modeled by a functional form of the type in (7). These authors

also provide a concise, illustrative comparison of Demkov and Landau-Zener models, which we

now compare and contrast.

The Demkov model, very briefly and very generally, posits that there is probability that

an electron transfer between diabats occurs at R_D when the value of H_{12} is approximately equal to

the energy gap, Δ, between the two states ($H_{12} = \Delta$, also, $H_{12} = \Delta/2$ [25]). Additionally, the behavior

of H_{12} before and after R_D relative to Δ determines whether the Demkov model is applicable.

These transitions typically occur for nearly parallel potentials commonly at larger interfragment

distance. Since this work expects attractive entrance channels paired with repulsive exit channels

from the single electron transfer described by strongly exothermic reactions (3)-(6), we expect

that the energy gaps at large R are likely to be significant and vastly larger than H_{12} ($H_{12} = 0.019$

eV at 7.94 Å in the ArN_2^+ system [24]) and that the behavior of H_{12} relative to Δ in the $Xe^{2+} + O_2$

collision system is not conducive to Demkov-type electron transfer.

In the general description of the Landau-Zener model, charge transfer occurs at critical

distances where the two non-adiabatic electronic states, product and reactant potential energy surfaces, cross one another. This distance, R_c, occurs when $\Delta = 0$, which is now the energy gap between diabatic curves at the crossing point. The simple existence of a crossing does not necessitate a surface hop; for hydrogen-like electrons, the Landau-Zener probability for a diabatic transition at the crossing distance is given as:

$$p_{LZ} = \exp\left(-2\pi[H_{12}(R_c)]^2/v_r\Delta F\right) \tag{8}$$

where $H_{12}(R_c)$ is the electronic coupling evaluated at the crossing distance, v_r is the radial velocity and ΔF, given here for a doubly-charged ion-neutral single electron transfer collision system, is the difference between the slopes of the diabatic curves at R_c given as:

$$v_r = v\left[1-\left(\frac{b^2}{R_c{}^2}\right)\right]^{\left(\frac{1}{2}\right)} \tag{9}$$

$$\Delta F \sim \frac{e^2}{R_c{}^2} \tag{10}$$

where v is the relative velocity of the collision system, e is the electronic charge and b is the impact parameter. Over the course of a typical collision trajectory, the particles pass through the crossing point two times. This leads to the transmission function, T, equal to:

$$T = 2p(1-p), \tag{11}$$

which is the ultimate probability that the system ends along the particular channel.

The introduction of diatomic species adds additional complexity beyond the "two-state" crossing model described above. Specifically, the nuclear degrees of freedom create additional entrance and exit channels at different asymptotic energies and which cross at different interfragment distances. Under the assumption that vibrational excitation does not perturb the ion-induced dipole entrance channels nor the repulsive exit channels beyond offsetting the asymptotic energies, the electronic coupling (7) is modified according to:

6

$$H_{12}^{v'v''} = H_{12}(<v'|v''>)^{(\frac{1}{2})} \tag{12}$$

where $<v'|v''>$ is the Franck-Condon factor for the two vibrational states of the specific electronic

states involved in the collision. As a result, the two-state crossing probabilities are now expanded

into a multi-channel Landau-Zener model (MCLZ) with various unique crossings and, in the case

of excited electronic states being involved, multiple different electronic coupling values.

Fukuroda et al. investigated one-electron capture processes using a matrix-based MCLZ scheme

for Ne^{2+} + H_2 to predict the vibrational population of resulting H_2^+ (X) products.[26] Lebius et al.

and Taulbjerg used MCLZ schemes to model triply- and highly-charged ion-atom charge transfer

reactions to connect to experimental results, respectively.[27, 28] Bauer et al. examined quenching of

excited sodium by molecular nitrogen using a potential grid surface similar to the approach taken

in this work and described below.[29] This work will attempt to expand such models to a product

distribution containing vibrational contributions from multiple electronic states.

The composition of the remainder of this paper is as follows: In Sec. II, we describe the

experimental apparatus to quantify the emission excitation cross sections for the two collision

systems studied. We also present a description of the spectral modeling used to obtain vibrational

populations for both electronic states of the O_2^+ product ion. Finally, we describe the specifics for

the MCLZ model used to predict the various vibrational states of the O_2^+ product ions. In Sec. III,

the experimental results and the spectral analysis for the O^+ + Xe and Xe^{2+} + O_2 collision systems

over a large collision energy range are presented. In Sec. IV, the results are discussed and

interpreted within the framework of the reaction window mechanism.

Experiment and methods

7

The experimental measurements are made using an ion beam-cell apparatus described previously and is only briefly summarized here.[7, 30] The ion beam is first generated using a radio frequency (RF) ion source (RFIS-100, Beam Imaging Systems). O^+ is generated from a mixture of carbon dioxide (research grade, Matheson Tri-Gas) and krypton gas (research grade, Advanced Specialty Gases) while Xe^{2+} ions are generated from xenon gas (research grade, Spectra Gases). The RF source was operated with gas pressure of ~100 milliTorr CO_2 and ~400 milliTorr of Kr for the O^+ studies. For Xe^{2+} ion generation, the xenon pressure was about 40 milliTorr. All generated ions are accelerated at a specified kinetic energy down the beam axis of the instrument and into a Wien filter, which selects for a particular mass-to-charge ratio. The mass-to-charge selected beam of ions, in this case O^+ or Xe^{2+} with an assumed statistical distribution of electronic states for Xe^{2+},[14] is then introduced to the collision cell containing the neutral target gas, Xe or O_2, held at a pressure of 1.2 mTorr, as measured by a capacitance manometer. Electronic excited states O^+ (^2D) and O^+ (^2P) lie ~3.32 and 5.02 eV above the O^+ (^4S) state. Low-energy electron impact sources operating with CO_2 have been shown to generate >98% pure ground state O^+ when operated within 1.5 eV above the appearance threshold of O^+; the actual electronic state distribution of O^+ used in this work was not directly measured.[31]

The target gas pressure is selected to keep the mean free path greater than the size of the collision cell. This is confirmed by the linear response of the luminescence signal to cell pressure. The selected ion beam kinetic energy is measured with a Retarding Potential Analyzer (RPA) and associated Faraday cup positioned beyond the back wall of the collision cell. The kinetic energy distribution for a particular beam energy is determined by sweeping the voltage of the retarding grid in the RPA and monitoring the beam current on the Faraday cup. The differential of the ion current with respect to applied voltage gives a line shape well modelled with a Gaussian profile.

At a beam energy of 500 eV in the laboratory frame (LAB), the full width half maximum (FWHM) of the kinetic energy of the beam is 35 eV, and at 6 eV (LAB) the FWHM is 4 eV. During the optical emission data collection described below, the total beam intensity is measured by simultaneously monitoring the current hitting the back wall of the collision cell and the Faraday cup while the retarding grid is set to 0 V.

Optical emission excitation spectroscopy is used to quantify the luminescence created by the collisions. The collision cell is connected to a fiber optic cable that transmits emissions to a spectrometer (Shamrock 303i, Andor Technology), which disperses and delivers the collected light to a charge-coupled device (CCD) (IDus DU-420, Andor Technology, 1024 x 255 pixels) operated in full-vertical binning mode. The spectral resolution of the experiment, set by the combination of the spectrometer slit width, dispersive power of the grating and pixel size of the CCD detector, is 0.8 nm, which is determined by measuring the FWHM of the Xe atomic lines in addition to the emissions of stand-alone pen lamps. The slit width of the spectrometer is set to 200 µm and experiments were performed using two different 600 lines per mm (ln/mm) gratings with blazes of 300 and 500 nm. In this configuration, it is possible to measure 110 nm per scan; multiple scans are required for a full spectrum at each collision energy. The CCD is operated in its linear dynamic range with the wavelength calibrated using known Xe neutral, Xe^+ and atomic O lines. Knowledge of the spectral sensitivity of transmission to and detection by the CCD is required to obtain quantitative emission excitation cross sections over the entire spectral region studied. The black body spectrum of a calibrated halogen-tungsten lamp is used to attain this spectral sensitivity curve above 450 nm. For the region below 450 nm, the detection sensitivity is determined using a calibrated deuterium lamp (SL3-Cal StellarNet Inc.). For selected collision energies another spectrometer and CCD are used to extend the spectra deeper into the UV (>200 nm). The 200 nm

limit of the deuterium lamp provides the short wavelength limit of the calibrated range. In this case the spectrometer (0.2 meter Scanning Monochromator, 234/302, McPherson) and the CCD camera (IDus DO420A-BN, Andor Technology) are both kept under high vacuum. The 1200 ln /mm grating combined with 1 mm slit opening disperses light from 30-550 nm with 3-3.5 nm spectral line width, determined with the atomic line in the deuterium lamp.

For the O_2^+ (b-a) emission band, the same experimental setup is used, except instead of a RF source, a direct current (DC) discharge source was used to create the ions. This source creates a discharge plasma between a hot filament and a metal anode held at typical voltages of 100 V for Xe^{2+}. A direct comparison of the two different sources measuring the same emission band yielded similar results at selected collision energies. Other collision systems, such as $Kr^+ + Kr$ and $Xe^+ + Xe$, gave similar emission excitation cross section energy dependencies when the two sources were also compared.

In all cases, the signal was corrected for background light levels, cosmic rays, and a varying geometrical factor, G, related to the effectiveness of the detection system in capturing photons from the collision. G is determined by reproducing previously measured $Xe^+ + Xe$ emission cross sections.[32] The absolute emission excitation cross section at a given detector pixel, λ, is given from the following equation:

$$\sigma_\lambda = \frac{q \cdot e \cdot J_\lambda}{I \cdot G \cdot P} \qquad (13)$$

in which q is the charge of the colliding ion, e is the electronic charge, J_λ is the integrated intensity (photons per unit time) at a particular pixel, P is the target gas pressure in the collision cell, and I is the total current of the ion beam. The cross sections for atomic lines are obtained by assuming Gaussian fits to the processed data and then converting to absolute cross section for a particular transition, $\sigma_{transition}$, found from integration over wavelength range where the atomic lines lie:

$$\sigma_{transition} = \int_x^y \sigma_\lambda d\lambda \quad . \tag{14}$$

In the case of the O_2^+ molecular transitions in the $Xe^{2+} + O_2$ collision system, which are not readily

fit with Gaussian profiles due to the complexity of the structure of the emission spectra, the cross

section is determined by performing a best-fit computer simulation, described below, and then

integrating the resulting cross sections over each specific emitting upper vibrational state.

For the modeling of the O_2^+ (*A-X*) and (*b-a*) manifold, an individual emission spectrum is

generated for each specific upper vibrational state using the diatomic constants for O_2^+ (*A*), (*b*),

(*a*) and (*X*) taken from Laher and Gilmore and references therein.[33] PGopher[34] is used to generate

21 basis functions for emission from each O_2^+ (*A*) *v'* upper state to the lower 11 vibrational states

for O_2^+ (*X* (*v''*)). This is also accomplished for 5 O_2^+ (*b*) states (*v'*) emitting to 11 O_2^+ (*a*) states

(*v''*). In order to generate a single basis function for each vibrational state of the excited electronic

state, individual transitions from the specific vibrational state to the various vibrational states of

the lower electronic state need to be weighted according to their expected contribution. The

weighting of an individual transition, $I_{v'}(v'')$, within the common upper state (i.e. 0←0, 1←0, 2←0,

.., *v''* ← 0) is scaled using:

$$I_{v'}(v'') = A_{21}^{v''v'} * I_{v'}^*(v'') \tag{15}$$

$$I_{v'} = \Sigma I_{v'}(v'') \tag{16}$$

where $A_{21}^{v''v'}$ is the Einstein coefficient associated with the *v''* ← *v'* transition, and the area under

the curve of $I_{v'}^*(v'')$ on the right-hand-side is initially unity. The individual basis function, $I_{v'}$, of

the O_2^+ (*A*) *v'* = 0 state, for example, is then the arithmetic sum of the 21 individual transitions (*v''*

= 0-21← *v'* = 0), where each has been multiplied by their respective weighting (Eqn. 15). Each

resulting $I_{v'}$ is then normalized such that its area is 1 for a common wavelength axis, which assumes

an equal fluorescence quantum yield from each respective upper vibrational state modeled in the limit of infinite detection time. The rotational temperature was estimated to be 300 K based on fits to isolated transitions in both the (*A-X*) and (*b-a*) emissions and is consistent with the combination of room temperature collision gas and expected long-range charge exchange. A line width of 0.8 or 3.4 nm, corresponding to the measured resolution of the experiment, was assumed for the simulations.

With the basis functions for the two electronic manifolds generated, a series of best-fit simulations are performed to minimize the chi-square value between the simulated spectrum and the scaled data. Fit parameters for the simulation include the population of each individual upper vibrational state and a single scale factor for each electronic band. The sum of the upper state populations are constrained such that their value must be unity. The scale factor then multiplies the entire resulting composite spectrum to best scale the simulation to the experimental data. For each upper vibrational state the reported population is the average value of the simulation attempts. For a single *v'* population, the value varied by 0.5-3% across the different ordered sets, except for those vibrational states that contain very little population. After obtaining the average populations at each collision energy, the vibrational state-specific emission cross sections are then readily calculated. For luminescence in the (*b-a*) region, spectra were fit over the 497 to 800 nm wavelength band while the (*A-X*) region was fit from 190-450 nm. For the O_2^+ (*b-a*) emissions, the mean-unsigned deviation in vibrational populations for *v'* = 0-3 was 2.7% over repeated, individual measurements at four collision energies.

Two custom multi-channel Landau-Zener model algorithms are used to make predictions about the resulting electronic and vibrational state after charge transfer occurs. In both frameworks of this model, the various entrance channel and exit channel potential surfaces are given as

$$V_{ent} = -\frac{q^2\alpha}{2R^4} + E_\infty \tag{17}$$

$$V_{exit} = \frac{1}{R} + E_\infty \tag{18}$$

where q is the charge of the ion on the entrance (*ent*) channel, α is the polarizability, R is the

interfragment distance and E_∞ is the asymptotic energy of the species. The MCLZ algorithm used

here differentiates between the polarizability of molecular oxygen when the ion approaches in a

perpendicular or parallel orientation relative to the O-O bond. The polarizability values used are

7.57 and 14.70 atomic units (a.u.). for perpendicular and parallel approach, respectively.[35] The

complete surface consists of 142 exit channels encompassing 21 vibrational states of O_2^+ (*X*), (*a*),

and (*A*) and the first 8 vibrational states of O_2^+ (*b*) and the two ground state Xe^+ products (Xe^+

($^2P^o_{3/2}$) and Xe^+ ($^2P^o_{1/2}$)). The first 11 vibrational levels of neutral O_2 (*X*) paired with Xe^{2+} ($^3P_{2,0,1}$,

^1D, ^1S) make up the 55 entrance channels. A composite figure of these potentials and a table of the

various asymptotic energies can be found in the supplemental information accompanying this

report. The first approach allows only a single transfer onto another surface, at which point the

channel is recorded. The second approach allows multiple transfer possibilities as the trajectory is

followed and is described in more detail next.

Trajectories were initiated at 93 different, equally-spaced impact parameter values ranging

from 0.1 to 9.3 Å with a user-specified, normalized population distribution of Xe^{2+} ions. For a

given impact parameter value, a straight line trajectory began along the x-axis 12 Å from the

center-of-mass of the oxygen molecule, defined as zero. Particles moved exclusively along the x-

axis (straight-line trajectory) and were either reflected at a specified cut-off distance (d_{inner}) or

continued until -12 Å along the x-axis if their minimum approach distance was greater than the

cut-off distance. All possible crossings between 12 Å and d_{inner} are calculated from the given input

parameters, sorted in decreasing distance order, and their specific impact parameter probabilities

are determined and recorded. For a given impact parameter, the simulation then proceeds through

all accessible crossing possibilities in both the approaching and departing directions. If a crossing

exists for exit channel i and entrance channel j, the probability of electron transfer is calculated

using eqn. (8) and the population-flux (C) of the relevant exit and entrance channel are recursively

modified as:

$$C_{exit,\ i} = \begin{cases} C_{exit,i} + C_{ent,j} * (1 - p_{LZ}) - C_{exit,i} * (1 - p_{LZ}) & b \le R_c \\ C_{exit,\ i} & b > R_c \end{cases} \quad (19)$$

$$C_{ent,j} = \begin{cases} C_{ent,j} + C_{exit,i} * (1 - p_{LZ}) - C_{ent,j} * (1 - p_{LZ}) & b \le R_c \\ C_{ent,\ j} & b > R_c \end{cases} \quad (20)$$

where ($1-p_{LZ}$) reflects that a single adiabatic transition is occurring. After updating the population-

flux in the respective exit and entrance channels, the simulation continues until another crossing

is encountered, eqns. (19) and (20) are evaluated again, and this process would continue as many

times as necessary until the interfragment distance reached |12 Å|. The initial flux of ions in a

specific impact parameter was determined assuming an equal density of ions through all space and

was approximated as:

$$C_{total,b} = \pi b_{current}^2 - \pi b_{prev}^2 \quad (21)$$

where $b_{current}$ and b_{prev} are the values of the impact parameter being investigated and the closest,

smaller preceding impact parameter value, respectively. Franck-Condon factors for the conversion

of O_2 (X) $\leftrightarrow$ O_2^+ (X, a, A, b) in equation (11) were again taken from Laher and Gilmore. H_{12} values

were calculated according to Olson et al.[22] (see their equations 7-12) where unique ionization

potential values for each electronic state of O_2 (X) $\rightarrow$ O_2^+ were used in the calculation of α (see

Olson et al.). These values were 0.4417, 0.5899, 0.6247 and 0.6659 a.u. for ionization into the O_2^+

(X), (a), (A) and (b) states, respectively.

Simulations were only initiated on five different entrance channels, those represented by

the Xe^{2+} ($^3P_{2,0,1}$, ^1D and ^1S) configurations paired with O_2 (X, $v = 0$). For the results detailed in this work, the Xe^{2+} (^3P) ions were assumed to have their expected ensemble ratio of 5:1:3. The weighting of (^3P:^1D:^1S) was calculated assuming a Boltzmann distribution with electron energy of 100 eV (Model 1), a 9:5:1 ratio (Model 2) and a 1:0:0 ratio (Model 3). For each exit channel (Xe^+ and O_2^+ product), the final C values expected for each impact parameter were integrated to give a total population, β. For the largest impact parameters, all exit channel C values result in zero contribution. Finally, the total population, β_{tot}, in a given state was taken as $\beta_{tot} = (2/3) \beta_\perp + (1/3) \beta_\parallel$. The processed results were then converted into state-specific cross sections and the populations of each O_2^+ (A) and (b) electronic state were normalized for comparison to experiment. An example depiction of this procedure appears in the supplemental information (Figure S4). No alteration to the straight-line trajectory was initiated as a result of successful charge transfer.

Simulations in which only a single hop was allowed were also performed. In these simulations, an electron transfer probability at each crossing for each vibrational state of O_2^+ was calculated using equations 7-12 for each impact parameter, examined with 0.1 Å resolution. The initial ion flux was distributed identically as described above. Successful charge transfer onto an exit channel at a specific crossing point decreased the remaining ion flux available at the next crossing. For a given impact parameter, the first crossing encountered was that with the greatest crossing distance, then the second greatest and so on. When the crossing at the smallest interfragment distance was completed, the simulation continued in reverse order (innermost to outermost). The O_2^+ populations and charge-exchange cross sections were then calculated by summation of the individual populations resulting from an impact parameter value of 0 to b_{max}.

Results

A. O^+ + Xe

Luminescence from the $O^+ + Xe$ system was measured at selected collision energy values in the range $E_{cm} = 14$ eV to $E_{cm} = 446$ eV. An example spectrum, for $E_{cm} = 446$ eV, is shown in Figure 1. The primary emissions observed between 750-1000 nm are assigned to electronically excited neutral O and neutral Xe. The higher noise level near 1000 nm is the result of the decreased spectral sensitivity of the detection system in this range, which necessitates a larger correction factor in the post-processing of the data. For atomic O, emissions at 777, 845 and 926 nm are observed corresponding to the upper electronic states: ^5P, ^3P and $^5D^o$, terms of the $3p^1$, $3p^1$ and $3d^1$ electronic configuration, respectively. For all three apparent emission lines, there are three to four contributing J terms that are not resolved at the resolution of the experiment. The emission excitation cross section values presented below are the sums of all contributors at each wavelength. Additionally, the lower electronic states of the 926 nm transitions serve as the upper states for the 777 nm emissions. For the atomic xenon emissions, transitions ascribed to the $2p_x$ (Paschen notation) electronic states are observed at 823, 828, 835, 882, 895, 905, 916, 980 and 992 nm.[32] The measured emission excitation cross sections for the transitions at 788 and 841 nm are less than 5×10^{-19} cm^2, determined by the baseline noise, and their emission excitation cross sections are not reported.

The collision energy dependence of the emission excitation cross section for selected atomic emissions in the 750-1000 nm range are shown in Figure 2. These cross sections have been determined according to the method described in the experimental section. Experimental error statistics for the emission excitation cross sections are based on two or three replicates performed for each energy. In the LAB frame, the collisional energy is in increments of 100 eV, with a finer resolution at lower energy. In Figure 2, measured cross sections from a selection of a single O emission line and three Xe emission lines are shown. At the lowest collision energy, the O emission

excitation signal level at 777 nm is indistinguishable from the noise. For all of the observed

emission lines, the emission excitation cross section increases with collision energy from 14 eV to

about 60 eV. Above 60 eV, the emission excitation cross sections are constant within experimental

precision, except for about a 30% reduction at E_{cm} = 446 eV for the O emission line at 777 nm.

The uncertainty is shown in Fig. 2 by repeated measurements. The measured emission excitation

cross sections across the collision energy range for the nine observed transitions from neutral Xe

($2p_x$, $5p^56p$) and the three transitions from O at 777 nm (^5P), 845 nm (^3P) and 926 nm ($^5D^0$) are

tabulated in Table 1.

B. $Xe^{2+} + O_2$

Figure 3 shows a typical luminescence spectrum over the 450-950 nm region for the Xe^{2+}

+ O_2 collision system, in this case for E_{cm} = 235 eV. This region includes the O_2^+ (*b-a*) emission

band as well as atomic emissions from neutral oxygen, neutral xenon and singly-charged xenon.

The progression starting above 500 nm and continuing to 800 nm is the band structure sequence

due to Δv = -2 to Δv = +4 where Δv refers to the difference in the vibrational quantum number of

the upper and lower states in the (*b-a*) transition. The narrow transitions observed at 777, 845 and

926 nm are emissions from atomic oxygen identical to those described above in the O^+ + Xe

section. The transition at 882 nm originates from neutral xenon while the narrow bands at 484 and

541 nm are due to emissions from Xe^+. The extended sequence at wavelengths below 450 nm is

due to the O_2^+ (*A-X*) manifold, which will be discussed below.

The energy dependence of spectrally integrated emission across the O_2^+ (*b-a*) band was

examined from approximately E_{cm} = 10 to E_{cm} = 941 eV. There are no statistically significant

alterations, greater than the experimental uncertainty, in the total emission excitation cross section over the entire sampled energy range for the O_2^+ (*b-a*) manifold. However, the experimental data have lower signal-to-noise at lower collision energies due to a reduced primary ion beam intensity which leads to increased uncertainties in the measured intensity. The O_2^+ (*b-a*) emission excitation cross-section energy dependence will be discussed in the next few paragraphs after presenting results of the modeling of the band. In contrast to the O_2^+ (*b-a*) cross sections, the atomic emission excitation cross sections do significantly change with collision energy. The atomic emissions become detectable above baseline at collision energies greater than E_{cm} = 59 eV and generally increase with increasing collision energy. The small values of the atomic emission excitation cross sections and the sparseness of the collision energies sampled precludes determining a threshold collision energy or conclusively determining a functional form of the energy dependence. Regardless of collision energy, transitions of these atomic species account for only a small fraction of the total emission excitation cross section in this spectral region.

Figure 4 shows a typical fit to the O_2^+ (*b-a*) manifold as described in the experimental section for E_{cm} = 9.8 eV. The data has been arbitrarily scaled to 1 while the residual at the top of the figure reflects the numerical difference between experimental data and the best fit. The fit included emissions originating in the electronic state with vibrational states up to *v'* = 6 with an allowed change in vibrational quanta of up to 5 and O_2^+ (*a*) as the final electronic state. The transitions from the individual vibrational states are not resolved in each band at the experimental resolution. The large positive going residuals seen in figure 4 near 484, 541, 777, 845 and 882 nm are the result of atomic emissions which are not modeled with the O_2^+ (*b-a*) basis functions. There are also residual emissions near the high energy side of the O_2^+ (*b-a*) transitions that show the fit is not completely quantitative. This likely results from the accuracy of the diatomic constants and

18

the assumption of a Gaussian lineshape for the convolution to the experimental resolution. As noted in the experimental section, a rotational temperature of 300 K appears to best describe the rotational envelopes of each band. The simulations derive populations of the individual vibrational states and the state specific cross sections of the O_2^+ (b) electronic state resulting from the charge-transfer reaction.

The strongest components of each Δv band are from $v' = 0$ and 1, with the exception of the $\Delta v = -2$ transitions where $v' = 0$ and 1 are prohibited from emitting into negative quantum numbers. Table II gives the absolute emission excitation cross sections for production of the individual vibrational state levels at the sampled collision energies based on fitting the experimental data at each respective energy. Additionally, selected atomic emission excitation cross sections are also included as well as an estimate of the lowest cross section that can be expected to be measured for an atomic emission based on the baseline level of the detection system. For the v' upper vibrational states, these cross sections reflect the upper vibrational state populated in the charge exchange reaction for the O_2^+ (b) electronic state. Cross sections for the individual vibrational states are as high as 200 x 10^{-18} cm^2 but tend to zero at higher upper state vibrational quantum number. The entirety of the emission excitation cross section for the O_2^+ (b-a) manifold can be obtained by summing the individual state-specific emission excitation cross sections. Figure 5 displays the total emission excitation cross section obtained by summing all eight upper vibrational state cross sections. The error bars indicate the standard deviation in repeated experiments. Over the range of collision energies, there is no change in the total emission excitation cross section beyond the apparent experimental uncertainty.

The population is dominated in vibrational states of $v' \leq 3$ with the majority in $v' = 0$ and 1 at all energies investigated. Figure 6 plots these vibrational states as normalized populations

along with the FC distribution. The FC distribution assumes an instantaneous and vertical process

for the population of O_2^+ (*b*) from ground vibrational state O_2 (*X*). In such a case, the probability

of populating a particular vibrational state in O_2^+ (*b*) is proportional to the overlap integral of the

vibrational wavefunction *v'* with the *v''* = 0 wavefunction of O_2 (*X*).[36] The fitted *v'* = 0 vibrational

population increases with increasing collision energy over at least the range of E_{cm} = 9.8 to 942

eV encompassing 43% of the total population of the *b* state at the lowest energy measured and

51% of the total population at 942 eV with a qualitatively smooth variance in between. The

population values for all energies are contained in Table S7 of the supplemental information

accompanying this report. Generally, the populations at all energies measured do not vary greatly

from the FC distribution, however, the *v'* = 0 population increasingly deviates as collision energy

is increased from its expected value of 41.1% of the population.

Luminescence originating from the O_2^+ (*A*) charge exchange product for the $Xe^{2+} + O_2$

collision system was acquired across a collision energy range from E_{cm} = 6 eV to E_{cm} = 233 eV.

Figure 7 shows an example spectrum and the best fit for the signal observed between 200 and 500

nm at E_{cm}= 233 eV. The vast majority of emission bands observed in this region are assigned to

O_2^+ (*A-X*) while minor products ascribable to electronic excited states of Xe^+ are also present.

Similar to the O_2^+ (*b-a*) manifold, individual rotational transitions are not resolved. Overlapping

emissions from multiple vibrational states occurring at similar wavelengths are also not resolved

at the experimental resolution. Fitting of the spectrum is required to acquire the O_2^+ (*A*) state

vibrational populations and state-specific cross sections.

The green trace in Figure 7 shows the resulting best-fit simulated spectrum for the

experimental data at E_{cm} = 233 eV. The abrupt cutoff at approximately 200 nm is a result of the

lack of calibration data for the deuterium lamp below this wavelength, as noted in the experimental

section. A best fit to the measured spectrum, shown in green, including the range of upper v' states from 0 to 21 gives excellent agreement with the measured data. The expected spectrum assuming a Franck-Condon distribution is also depicted, in blue, to allow a more direct comparison.[19] The best fit simulation generates greater populations in the lower vibrational states leading to stronger emissions in the near-visible side of the spectrum while decreasing the deep ultraviolet emissions from the higher vibrational states.

Figure 8 shows the resulting simulated populations derived from the spectra measured at three different collision energies, E_{cm} = 37, 59 and 233 eV. Error bars are the standard deviation of 10 different, unique simulations in which the basis function order has been randomized. All spectra show population maxima near v' = 8 and 9. There are also populations nearby that have significant intensity in the fits, as shown by the error bars. An analysis of the emissions expected to be the most intense for each basis function shows that there is significant overlap for the highest v' states, particularly in the 200-240 nm region. This overlap contributes to the large reported error bars for v' > 15 where a unique combination of basis functions is not possible at the experimental resolution. In all cases, the populations of the lowest vibrational states are significantly over-represented when compared to the FC distribution.

At the highest collision energy measured, 233 eV, the vibrational state distribution has subtle broadening even to populations at v' = 20 and 21 and becomes the most similar to the FC distribution. As Fig. 8 shows, the spectrum still has portions that are significantly different than the FC distribution, particularly near 250 nm and the higher intensity of transitions above 300 nm. Generally, at the lowest collision energy measured with this detection setup, the vibrational population appears to prefer higher lying vibrations than the FC distribution which gradually approaches the FC distribution as collision energy is increased. Quantitatively, the weighted

average of population multiplied by the vibrational quantum can provide insight into the differences from the FC distribution for each distribution. The weighted average of the populations are 9.38, 8.76 and 8.34 for the 37, 59 and 233 eV collision energies, respectively, while the FC distribution is 8.36. The change in this summed number does suggest movement to the FC distribution, which is less evident when comparing the individual vibrational populations.

Figure 5 shows the collision energy dependence of the emission excitation cross sections for the O_2^+ (*A-X*) manifold. The O_2^+ (*A-X*) emissions are tabulated in two different ways. The first uses the summed emission excitation cross section values in the region of 327 to 423 nm, a subset of the entire band. The solid squares are the cross sections augmented by the fits to the experimental data. The fit to the data mitigates experimental difficulties, such as the cut-off at 200 nm or the overlapping of bands in the visible with the O_2^+ (*b-a*) transitions. The whole band values should be considered to be the expected emission excitation cross section encountered over the 175-1000 nm optical range. For the subset, the cross sections are constant within the error bars across the larger collision energies with the summed cross section approximately 100 x 10^{-18} cm^2 (1 Å^2) over the entire sampled range of E_{cm} = 6-191 eV. The reproducibility for these cross sections give standard deviations better than 20%. Table III shows a sample of some of the state-specific cross sections assuming the vibrational populations derived solely from the fit of the experimental data. The largest vibrationally state-resolved cross sections are of the order of 10-100 x 10^{-18} cm^2. The integrated O_2^+ (*A-X*) emission excitation cross sections appear larger than the integrated O_2^+ (*b-a*) emission excitation cross sections at all collision energies measured. The emission excitation cross section for the O_2^+ (*A-X*) band appears invariant with collision energy over the range measured and has values between 600-800 x 10^{-18} cm^2 (6-8 Å^2).

An initial, restricted LZ model, which allowed only a single electron transfer, was

22

attempted that included production of the O_2^+ (*A*), (*b*), (*a*) and (*X*) electronic states. The prevalence of O_2^+ (*A*) crossing points below 3.5 Å, where H_{12} and, subsequently, *T* values are large, results in very large charge exchange cross sections for generation of products in the O_2^+ (*A*) state. The simulation attempted to best model the data set consisting of 8 collision energies spanning E_{cm} = 9.8 to 942 eV. The evaluation was limited only to minimizing the summed differences, calculated via the least-squares method (χ^2_{min}), in normalized vibrational populations between experiment and simulation within the O_2^+ (*A*) and (*b*) electronic states; the cross sections were calculated as a result of the best vibrational fit. Best fit simulation parameters are given in Table IV. There are numerous other minima within one multiple ($2\chi^2_{min}$) of the global best least-squares value, each with often significantly different H_{12} values. In all cases, the O_2^+ (*A*) state state-specific charge exchange cross section appears to be in the 20-40 Å² range, significantly larger than the emission excitation cross section measured. For the best fit parameters assuming Model 1 populations, the O_2^+ (*b*) state charge-transfer cross section decreases from ~8.1 Å² at 9.8 eV to ~1.3 Å² at 942 eV; the O_2^+ (*A*) state charge-transfer cross section decreases from ~28 to ~11 Å² over the same energy range.

The role of multiple electron transfers during the course of a trajectory was examined using the unrestricted multi-channel LZ model. In this model, no restrictions on the number of different electron transfers were placed on a single trajectory. The closest approach allowed between the two fragments, d_{inner}, was simulated from 2.0 to 4.1 Å. One illustrative example of the simulation outputs is presented in Figure 9 where the H_{12} values of all 4 electronic states were initially scaled identically and the *B* parameter was fixed to 0.86 for all 4 electronic states. Similar to above, the simulation figure-of-merit is the least-squares difference in normalized vibrational state for the two measured electronic states, O_2^+ (*A*) and (*b*). Figure 9 depicts the least-squares

values of both the O_2^+ (*A*) and (*b*) state populations and their respective charge-exchange cross section values as a function of d_{inner} and the H_{12} scaling parameter, *A* (eqn. 7), for a single collision energy, E_{cm} = 37 eV and with d_{inner} ranging from 2.8 to 4.1 Å. Panels c) and d) assume that charge-exchange into the state correlates directly to emissions out of that state. For this single collision energy, minima are observed between 3.1-3.2, 3.4-3.7 and 3.8-4.1 Å with a scaling parameter near one for the O_2^+ (*b*) state and near 3.6 Å and *A* = 2 for the O_2^+ (*A*) state. Good agreement between experimental emission and simulated charge-exchange cross sections is found along scaling parameter values around 0.75 for the entire 2.8-4.0 Å cut-off sampling.

The scaling parameters *A* and *B* for the O_2^+ (*a*) and (*X*) states have no direct link to measurements made in this report as the two states do not fluoresce. As a result, there is no direct metric to determine the reasonableness of determined values. However, the O_2^+ (*a*) state must be included as calculated charge-exchange cross sections in between the O_2^+ (*A*) and (*b*) values are regularly determined, and it appears to have a significant role in removing population from the O_2^+ (*A*) state. A random sampling of the parameters was undertaken examining the phase space that includes the *A* parameters for all four O_2^+ electronic states sampled where the *A* parameter for all O_2^+ states ranged from 0.1-6.0 and the *B* parameter was varied between 0.5 and 1.5. The d_{inner} parameter was allowed to vary between the set that includes the ranges 2.0-4.0 for a single collision energy of 37 eV. For each of the 30,000 different random configurations generated within these ranges, the metric of interest was the sum of the least-squares values for the normalized populations of both O_2^+ (*A*) and (*b*). Additionally, we required that the simulated charge exchange cross sections be within a factor of 2 of the experimental emission excitation cross section values at this collision energy. The 1200 sampled parameters with the best least-squares values were then simulated over six collision energies and the result of the lowest

combined least-squares value is presented in the four rightmost columns of Table IV. The numbers appearing underneath the parameters indicate the range where the cross section and population least-squares differences remains below two separate thresholds. The first threshold is that the χ^2_{min} value associated with the energy dependence of the charge-exchange cross section into O_2^+ (*b*) is still within a factor of 2 of the value obtained with the best simulated parameter set. The second threshold is that the χ^2_{min} value for the energy dependence of the O_2^+ (*b*) populations remains within 1.5 times the value obtained for the best simulation parameters. It is again assumed that charge-transfer into O_2^+ (*b*) results in radiative emission from the state. This sensitivity analysis was only performed along one parameter at a time; the other parameter values were kept at their best values.

A cut-off value of 3.1295 Å was found for the parameter set with the best energy dependence for both the populations and cross sections. The simulated populations predicted by the parameter set for the O_2^+ (*b*) state are shown in Figure 6. The model, similar to the experimental results, predicts an increase in the *v'* = 0 population with increasing collision energy. The model nearly quantitatively reproduces the *v'* = 0 populations while consistently over-emphasizing the *v'* = 1 population and under-estimating the *v'* = 3 population. For this parameter set, the charge-exchange cross-sections into the O_2^+ (*b*) state were 3.74 Å^2 at 9.8 eV and 3.66 Å^2 at 941 eV. Similarly the O_2^+ (*A*) and (*a*) states varied from 9.7 → 5.1 Å^2 and 2.7 → 1.0 Å^2, respectively. The Xe^{2+} (^3P, ^1D and ^1S) ions contribute approximately 35, 64 and 1.0% of the total charge exchange cross section, respectively, assuming a Boltzmann distribution generated by an electron energy of 100 eV (Model 1). Model 2, which adopts a 9:5:1 ratio for the (^3P:^1D:^1S) parent ions, gives the same parameter set as the best answer. The combined χ^2_{min} value for the populations into the O_2^+ (*A*) and (*b*) was 1.5% lower than Model 1. The least-

squares difference associated with the energy-dependence of the charge-transfer cross section into the O_2^+ (*b*) state approximately doubles relative to Model 1, again assuming charge-exchange into the state results in radiative emission out of the state. The best parameter set identified for the input population used in Model 3 (*³P* ions only) results in a combined population χ^2_{min} value 50% larger than Model 1. The least-squares difference for the energy dependence of the charge-transfer/emission cross-section is a factor of 8 times larger than the value obtained with population Model 1.

Discussion

A. O^+ + Xe

The luminescence spectrum in the 750-1000 nm range from the O^+ + Xe collision system contains primarily neutral, atomic O and Xe species. The presence of the neutral O is the result of a charge-transfer reaction that generates electronically excited products. Emissions resulting from excited O electronic states are produced from an endothermic process. Emissions were not observed for neutral, atomic oxygen products at E_{cm} = 14 eV but are apparent by 29 eV, the next energy measured. The coarseness of the measured values prohibits the assignment of a threshold but the results are not inconsistent with the endothermic charge exchange reaction:

$$O^+ \, (^4S^o) + Xe \, (^1S) \rightarrow O \, (^5P) + Xe^+ \, (^2P^o) \quad \Delta H = +9.25 \text{ eV}. \qquad (21)$$
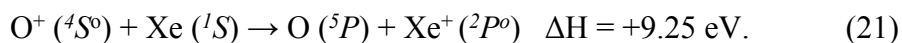
While the emission excitation cross section is on the order of tens of 10^{-18} cm², the value would still result in a small charge-exchange cross section, 0.4 Å² above 100 eV, consistent with a small impact parameter requiring high collision energy. Neutral Xe emissions are due to small-impact parameter inelastic collisions and are comparable to previous cross section measurements of the same states resulting from Xe^+ + Xe collisions.[32] The cross sections for excited Xe resulting from O^+ + Xe collision are about 40-60% of the previous Xe^+ + Xe measurements for the same

transitions.[37] For cross sections less than 5×10^{-18} cm^2, the differences are reduced but accuracy

of these values are also less certain. Also, the ratio of the 882 to the 823 nm cross sections in the

Xe$^+$ + Xe reaction and the O$^+$+ Xe reaction are relatively constant with a ratio of approximately

2. The energy dependence of the neutral xenon emissions appears to move in concert for all of

the states measured. As a result, inclusion of near-infrared emissions from neutral Xe resulting

from O$^+$ + Xe energetic collisions are not expected to alter interpretation of ion thruster models.

These collisional radiative models derive electron temperatures from ratios of emission lines.[17]

B.   Xe^{2+} + O$_2$

The large emission excitation cross sections for both O$_2^+$ (*A-X*) and (*b-a)* manifolds

suggest exothermic charge transfer into the (*A*) and (*b*) states. For both of the reactions, upper state

vibrational state populations deviate from FC distributions at all collision energies. Rotational

population analysis suggests internal rotational energy is unchanging with collision energy and is

reasonably well described by a ~300K distribution. These results are similar to those observed in

the previous luminescence study of Xe^{2+} + N$_2$, and thus, the explanation is similar, namely, long-

range charge transfer occurs in a region of the potential with little angular anisotropy as is thus

inefficient at generating torque required to affect the rotational state.[7] Both this study and that of

Xe^{2+} + N$_2$, are consistent with thermal experiments by Smith *et al.* that found production of N$_2^+$

with near complete collisional efficiency for both the (^3P) and ($^1D_2$) electronic states of Xe^{2+}.[7] At

the collision energies used in this work, a direct mechanism is assumed, as was found in cross

beam work of Herman of single-electron transfer of doubly charged ions.[38]

As observed in Figures 6 and 8, the vibrational populations for both O_2^+ (A) and O_2^+ (b) deviate from a FC distribution. Previous studies on the $Ar^{2+} + N_2$ system as well as the $Xe^{2+} + N_2$ system found that efficient charge transfer is observed when there is a curve crossing between the reactant and product state potential with intermolecular distances between 3 and 6 Å.[9, 13, 14, 16, 39] In an analysis of nearly 20 doubly-charged-neutral collision systems, Lindinger found the fastest rate coefficients for those crossings occurring nearest to 4 Å.[13] Figure 10 depicts some of the relevant intermolecular curve crossings for the $Xe^{2+} + O_2$ system. The potentials shown are Coulombic potentials of the $Xe^+ (^2P_{3/2,1/2}) + O_2^+$ (A,b) for the products and long range ion-induced dipole potentials for reactants of $Xe^{2+} (^3P_{2,1,0}) + O_2(X)$. The ion-induced dipole potentials are identical to those generated using eqn. 17 although α is now the isotropic oxygen polarizability. All (^3P) spin-orbit states of Xe^{2+} have crossings, in a perpendicular approach, with ground vibrational O_2^+ products in the 2-6 Å region with crossings for the $Xe^+ (^2P_{3/2}) + O_2^+$ ($v = 0$) products at 3.82, 3.12 and 3.03 Å for the (A) state and 5.21, 3.92 and 3.73 Å for the (b) state. Xe^{2+} (^1D) crossings into the $Xe^+ (^2P_{3/2, 1/2})$ products occur for the O_2^+ ($b, v = 0$) and ($A, v = 0$) states at (3.14, 4.11 Å) and (3.29, 2.66 Å), respectively. For the same approach orientation and products, Xe^{2+} (^1S) ions cross at 2.69 Å and 2.37 Å. Each of the O_2^+ electronic states thus have crossings between 2 and 6 Å; therefore, there is an expectation of significant production of low v products for both excited electronic states measurable in this work. These qualitative predictions agree with the results of fits to the measured spectra, which show significant population of the lowest vibrational states at all collision energies.

Advancing beyond qualitative, we attempted a number of electron transfer models based on Landau-Zener theory in an effort to quantitatively predict the vibrational populations and charge exchange cross sections resulting from single electron charge exchange processes. Specifically,

we investigated *i)* a reduced LZ model that incorporated vibrational states from all four O_2^+ charge exchange products and a single electron transfer was allowed and *ii)* a more complex LZ model which allowed any number of possible electron transfers including all four O_2^+ electronic states and the first 11 vibrational levels of ground-electronic state molecular oxygen. The O_2^+ (*b*) vibrational populations provide advantages in modeling when compared to the O_2^+ (*A*) state owing to the reduced number of available vibrational states, improved resolution of the vibrational states in the experimental spectrum and the reduction of overlapping emissions from different upper vibrational states. We also attempted to significantly alter the relative distributions of Xe^{2+} ions beyond that predicted by a Boltzmann distribution, including adopting a 9:5:1 distribution for (*³P*), (*¹D*) and (*¹S*) in addition to assuming only (*³P*) ions prior to collision.[14] Ultimately, we were able to reproduce the energy dependence of the O_2^+ (*b*) vibrational populations using both LZ models and all three population distributions with variously different scaling and cut-off parameters. For one example, the energy-dependence of the *v* = 0 vibrational population in the experimental data is always qualitatively captured in the Landau-Zener models attempted; a smaller relative population at the lowest velocities progresses to a large relative population at the higher velocities. For different valued parameters, the population alters too much, too little or is just right with velocity changes.

Notably, as the model complexity progressed from *i)* to *ii)* the innermost interfragment distance required to generate the best-fit populations shifted, only slightly, from 3.1 to ~3.13 Å. If an assumption is adopted that all O_2^+ (*b*) produced through charge exchange in the model results in O_2^+ (*b-a*) fluorescence, the simplest model generally overestimates the cross section (~8 Å² at E_{cm} = 9.8 eV) and expects a cross section value that decreases by a factor of 6 at E_{cm} = 942 eV. The full MCLZ model reasonably produces the correct value and its energy dependence. For the

O_2^+ (A) state, model i) estimates charge-exchange cross sections of nearly 28 Å^2 at E_{cm} = 9.8 eV

to 11 Å^2 at E_{cm} = 942 eV while model ii) predicts values of 9.7 to 5.1 Å^2 over the same range (for

d_{inner} = ~3.13 Å).

The modeling required an arbitrary inner cut-off for those trajectories occurring with small

impact parameters. We must acknowledge that this cut-off appears ad-hoc; the combined atomic

radius of atomic oxygen and atomic xenon is ~1.68 Å, the approximate combined covalent radius

is ~2.03 Å and the combined Van der Waal's radius is expected to be about 3.4 Å when using the

radius for Xe$^+$. We might speculate that at some small interfragment distance, the coupling must

be large enough that avoided crossings should result or interactions with the repulsive wall of the

XeO^{2+} complex must occur. For both model i) and ii) a larger inner cut-off radius facilitates the

removal of potential crossings from the Xe^{2+} (^1S) ion which generally occur in the 1.6-3.0 Å

window. Our sampling approach included potential cut-off distances down to 2.0 Å. Typically

small d_{inner} values resulted in output v' = 0 populations for O_2^+ (b) that were too small and a much

larger population in the larger vibrational quantum numbers than measured in experiment. We also

note that the number of successful hops from channel to channel vastly increases as the inner cutoff

is decreased which results in a smoothing of the populations in all of the electronic states. The

identified best-fit parameters appear to best reproduce the O_2^+ (b) and (A) vibrational populations

and the energy-dependence of the charge-transfer-to-emission-excitation cross section for O_2^+ (b)

while somewhat reproducing the energy dependence of the same cross-section for O_2^+ (A). Other

A and B parameters at longer cut-off distances could reproduce the populations as well, but could

not reproduce the invariance of the energy dependence of the experimentally measured O_2^+ (b)

emission cross sections. That suitable agreements between simulated population and experimental

population for various models and numerous different parameter values is found indicates that we

must exercise caution in deriving meaning from arbitrary cut-offs. The available experimentally measured results are simply not of high enough quality to make definitive conclusions on the ion-neutral closest approach distances. We do note, however, that Adams et al. find the reactivity of the Xe^{2+} (^1S) ion to be significantly reduced when compared to the (^3P) and (^1D) ions; this is clearly reflected in the multi-hop model when compared to the single-hop models where only about 1% versus 60% of the charge-transfer cross-section results from (^1S) parent ions.

There are a number of conflicting factors, unmeasured in this work, that make assuming O_2^+ ions produced by charge exchange into excited electronic states directly translate into fluorescence from those excited states. Adams et al. have previously reported that 40% of ions produced from collisions of Xe^{2+} (^1D) with O_2 at thermal velocities result in O^+ products. The presence of excited atomic neutral oxygen lines in Figure 3 indicates that dissociation, whether dissociative charge-transfer or small-impact parameter inelastic collisions leading to dissociation, are occurring at least at high collision energies. Higher lying vibrational states of both O_2^+ ($A, v > 11$) and ($b, v > 3$, or $v > 7$ in Erman and Larsson) are known to pre-dissociate, thus reducing their radiative emissions and emission cross-sections.[40-42] In the Xe^{2+} + O_2 system, charge exchange, in the Landau-Zener framework, into high vibrational states of O_2^+ (b) typically occur at large interfragment distances with low probabilities. As a result, pre-dissociation is not expected to have a significant influence on measurements reported here since this electronic state is well modelled by including only the lowest vibrational numbers. In contrast, effective modeling of the O_2^+ (A-X) emission spectrum requires population in all 22 vibrational quanta of O_2^+ (A) included in the analysis. The radiative lifetime of the O_2^+ (A) states ranges from ~600-1020 ns for $v = 0$ to 1550 ns for $v = 20$.[42-44] We were unable to locate any reports that could provide insight into the relative rates for radiative relaxation compared to the pre-dissociative relaxation for this electronic

state. As a result, we cannot quantitatively determine how much potential radiative loss should be expected for the O_2^+ (*A*) state. The simulated charge-transfer cross sections also find that Xe^{2+} (*^1D*) ions preferentially result in population into the highest vibrational states of both the O_2^+ (*A*) and (*a*) states for the best fit parameter values found here whereas the (*^3P*) ions typically populate the lower vibrational states,

Two final considerations that would influence the measured emission cross sections should be addressed. These two considerations relate to loss of ions to collisions with the collision cell walls and potential issues with calibrations. For single electron transfer occurring in doubly-charged-neutral collision systems at very low relative velocities, electron transfer at short distances can lead to large velocities of the newly formed product ion. For example, for Xe^{2+} ions traveling at a laboratory energy of 1 eV (E_{cm} = ~0.20 eV) and exchanging an electron at 2.5 Å results in an approximate O_2^+ laboratory velocity of ~4.3 km/s resulting from the Coulombic interaction, assuming the particles can be treated as point charges. The same situation with a 100 eV Xe^{2+} ion results in an oxygen ion laboratory velocity of about 1.4 km/s. The collision cell used in this work is approximately 2.54 x 10^{-2} m. If the center of the cell is taken as the mean distance where ions are formed, it takes approximately 9.1 µs for an ion traveling at 1.4 km/s to impact the walls of the cell. The radiative lifetimes of the various vibrational states of O_2^+ (*A*) are sufficiently short that only 0.2% of the molecules, at 1.4 km/s, with v = 21 initial state should be lost to collision with the walls. The O_2^+ (*b*) state has longer radiative lifetimes. For the same product velocity, approximately 0.5% of the initially created ions with v = 4 should be lost to collisions with the walls. At 4.3 km/s, 12.5 and 17% of the ions in the same respective vibrational states are expected to be lost to collisions with the walls, again assuming a crossing distance of 2.5 Å. The densities

in the collision cell are such that the mean-free path is longer than the length of the collision cell making collisions with the wall more likely than collisions with other particles.

The broad wavelength range over which the O_2^+ (*A-X*) emissions occur presents some difficulty to absolute measurements of the emission excitation cross sections. Our analysis utilizes calibrated broadband lamps and a calibration collision system believed to be accurate to within about 40%. We have previously been able to reproduce published electron impact results involving CO_2 and vacuum ultraviolet emissions from Xe over wide energy ranges. We appear to have agreement regarding the magnitude of the emission excitation cross section for NH/ND (*A-X*) occurring in the 320-340 nm range resulting from the collision with essentially any atomic, ionic collision system.[45-47]

Conclusions

The collisional energy dependence of luminescence generated in the 250-1000 nm range for reactions of Xe^{2+} + O_2 (*X*) from E_{cm} = 9.8 to 940 eV was examined under single collision conditions. The dominant emissive products are assigned to excited electronic states of O_2^+, specifically the (*A-X*) and (*b-a*) transition bands. The production of O_2^+ is the result of long-range exothermic charge transfer, demonstrated by the collision energy independence of the cross section as well as the lack of rotational excitation in either product. The vibrational states of O_2^+ (*b*) tend to be preferentially populated in v' = 0 and 1, with an energy variation well modeled from Landau-Zener probabilities. The vibrational states of O_2^+ (*A*) are spread over a wide range of vibrational states up to v' = 21. The energy-dependence of these populations also appear to follow predictions from Landau-Zener theory but the quality of experimental data makes this less definitive. The total

emission excitation cross sections for O_2^+ (*b-a*) and (*A-X*) are approximately constant within experimental uncertainty over the examined collision energy range. Vibrational populations suggest the majority of charge-transfer transitions occur at crossings between the long-range attractive ion-induced dipole potentials of the reactants and the repulsive Coulomb potentials of the products between $3 - 6$ Å from all three spin-orbit states of Xe^{2+} (*³P*) and the Xe^{2+} (*¹D*) excited ions. If the fluorescence yield for emissions from O_2^+ (*b-a*) and (*A-X*) is directly correlated to charge-transfer into O_2^+ (*A, b*), the modeled behavior of the emission excitation cross sections requires the introduction of an innermost approach cut-off value into the model to reproduce the experimental results. In a single hop Landau-Zener model, the expected charge transfer cross section at 9.8 eV is expected to be ~58 Å² with ~50% resulting in O_2^+ (*A*) formation, for a single-transfer model with an inner cut-off at ~3.1 Å and Xe^{2+} (*³P:¹D:¹S*) ions in a Boltzmann distribution created via electron impact with energy of 100 eV. This model predicts significant decrease in the charge-transfer cross-sections with increasing collision energy (~60% decrease for in O_2^+ (*A*) formation) by 941 eV. The best matching multi-hop Landau-Zener model reproduces the energy dependence of the vibrational populations of both O_2^+ (*A*) and (*b*) and the emission excitation cross-section originating from O_2^+ (*b*) but slightly overestimates the expected decrease in cross section with increasing collision energy for O_2^+ (*A*). The total cross section at $E_{cm} = 9.8$ eV is ~16 Å² and 9.8 Å² at $E_{cm} = 471$ eV.

The luminescence experiments of $O^+ + Xe$ yielded transitions, in the 750-1000 nm range, from both excited state Xe and neutral O. The observed cross sections of the neutral Xe emissions in the near infrared have magnitudes approximately half of the values at similar collision energies as compared to those resulting from $Xe^+ + Xe$. The energy dependence of the emission excitation cross sections for these transitions indicate that they increase similarly as collision energy is

increased. As a result, ratios of the lines are expected to move identically above threshold. This threshold was not measured in this work but occurs before E_{cm} = 14.3 eV for neutral Xe. Since the ratios move identically, the contribution of energetic O^+ + Xe collisions to Xe 2p (Paschen) emissions is not expected to alter interpretation of collisional-radiative models in the near infrared.

Conflicts of Interest

There are no conflicts to declare.

Acknowledgements

References

1. S. M. Andrews and L. Berthoud, presented in part at the 70th International Astronautical Congress (IAC), Washington D.C., United States, 2019.
2. O. Tumuklu and D. A. Levin, *Journal of Spacecraft and Rockets*, 2018, **55**, 1154-1165.
3. A. J. R. Lopez-Arreguin and E. Stoll, *Results in Physics*, 2019, **14**, 102442.
4. M. J. Bastian, R. A. Dressler and E. Murad, *The Journal of Chemical Physics*, 1995, **103**, 144-149.
5. R. A. Dressler, J. A. Gardner, R. H. Salter and E. Murad, *The Journal of Chemical Physics*, 1992, **96**, 1062-1076.
6. A. Ehbrecht, N. Mustafa, C. Ottinger and Z. Herman, *The Journal of Chemical Physics*, 1996, **105**, 9833-9846.
7. B. D. Prince and Y.-H. Chiu, *The Journal of Chemical Physics*, 2011, **135**, 104308.
8. Y. C. Chang, Y. Xu, Z. Lu, H. Xu and C. Y. Ng, *The Journal of Chemical Physics*, 2012, **137**, 104202.
9. S. D. Price, *Journal of the Chemical Society, Faraday Transactions*, 1997, **93**, 2451-2460.

10.   E. Y. Kamber, K. Akgüngör, C. P. Safvan and D. Mathur, *Chemical Physics Letters*, 1996, **258**, 336-341.

11.   E. A. Gislason and G. Parlant, *Comments on Atomic and Molecular Physics*, 1987, **19**, 157.

12.   T. R. Govers, P. M. Guyon, T. Baer, K. Cole, H. Fröhlich and M. Lavollée, *Chemical Physics*, 1984, **87**, 373-387.

13.   W. Lindinger, *Physica Scripta*, 1983, **T3**, 115.

14.   N. G. Adams, D. Smith and D. Grief, *Journal of Physics B: Atomic and Molecular Physics*, 1979, **12**, 791.

15.   R. Johnsen and M. A. Biondi, *Physical Review A*, 1978, **18**, 996-1003.

16.   D. Smith, N. G. Adams, E. Alge, H. Villinger and W. Lindinger, *J. Phys. B*, 1980, **13**, 2787.

17.   A. D. Rainer, C. Yu-hui, Z. Oleg, B. Klaus, S. Rajesh and S. Lalita, *Journal of Physics D: Applied Physics*, 2009, **42**, 185203.

18.   S. Jullien, J. Lemaire, S. Fenistein, M. Heninger, G. Mauclaire and R. Marx, *Chemical Physics Letters*, 1993, **212**, 340-346.

19.   F. R. Gilmore, R. R. Laher and P. J. Espy, *Journal of Physical and Chemical Reference Data*, 1992, **21**, 1005.

20.   Y. U. Demkov, *Journal of Experimental and Theoretical Physics*, 1964, **18**, 138.

21.   C. Zener and R. H. Fowler, *Proceedings of the Royal Society of London. Series A, Containing Papers of a Mathematical and Physical Character*, 1932, **137**, 696-702.

22.   R. E. Olson, F. T. Smith and E. Bauer, *Appl. Opt.*, 1971, **10**, 1848-1855.

23.   M. Kimura, T. Iwai, Y. Kaneko, N. Kobayashi, A. Matsumoto, S. Ohtani, K. Okuno, S. Takagi, H. Tawara and S. Tsurubuchi, *Journal of the Physical Society of Japan*, 1984, **53**, 2224-2232.

24.   P. Archirel and B. Levy, *Chemical Physics*, 1986, **106**, 51-68.

25.   A. Bárány and D. S. F. Crothers, *Physica Scripta*, 1981, **23**, 1096-1103.

26.   A. Fukuroda, N. Kobayashi and Y. Kaneko, *Journal of Physics B: Atomic, Molecular and Optical Physics*, 1989, **22**, 3457-3469.

27.   H. Lebius, H. R. Koslowski and B. A. Huber, *Zeitschrift für Physik D Atoms, Molecules and Clusters*, 1989, **11**, 53-61.

28.   K. Taulbjerg, *Journal of Physics B: Atomic and Molecular Physics*, 1986, **19**, L367-L372.

29.   E. Bauer, E. R. Fisher and F. R. Gilmore, *The Journal of Chemical Physics*, 1969, **51**, 4173-4181.

30.   Y.-H. Chiu, B. L. Austin, S. Williams, R. A. Dressler and G. F. Karabadzhak, *Journal of Applied Physics*, 2006, **99**, 113304.

31.   Y.-h. Chiu, R. A. Dressler, D. J. Levandier, S. Williams and E. Murad, *The Journal of Chemical Physics*, 1998, **109**, 5300-5307.

32.   J. D. Sommerville, L. B. King, Y.-H. Chiu and R. A. Dressler, *Journal of Propulsion and Power*, 2008, **24**, 880.

33.   R. R. Laher and F. R. Gilmore, *Journal of Physical and Chemical Reference Data*, 1991, **20**, 685.

34.   C. M. Western, *Journal of Quantitative Spectroscopy and Radiative Transfer*, 2017, **186**, 221-242.

35.   T. D. Poulsen, P. R. Ogilby and K. V. Mikkelsen, *The Journal of Physical Chemistry A*, 1998, **102**, 8970-8973.

36.   D. C. Jain and R. C. Sahni, *International Journal of Quantum Chemistry*, 1968, **2**, 325-332.

37.   E. Clementi, D. L. Raimond and W. P. Reinhardy, *The Journal of Chemical Physics*, 1967, **47**, 1300.

38.   Z. Herman, *International Reviews in Physical Chemistry*, 1996, **15**, 299-324.

39.   B. D. Prince and Y.-H. Chiu, *J. Chem. Phys.*, 2011, **135**, 104308.

40.   A. Carrington, P. G. Roberts and P. J. Sarre, *Molecular Physics*, 1978, **35**, 1523-1535.

41.   J. C. Hansen, M. M. Graff, J. T. Moseley and P. C. Cosby, *The Journal of Chemical Physics*, 1981, **74**, 2195-2200.

42.   P. Erman and M. Larsson, *Physica Scripta*, 1977, **15**, 335-338.

43.   R. W. Wetmore, J. L. Fox and A. Dalgarno, *Planetary and Space Science*, 1984, **32**, 1111-1113.

44.   M. Jeunehomme, *The Journal of Chemical Physics*, 1966, **44**, 4253-4258.

45.   B. D. Prince, C. P. Steiner and Y.-H. Chiu, *The Journal of Chemical Physics*, 2012, **136**, 144314.

46.   R. Drozdowski, S. Werbowy, Ł. M. Sobolewski and A. Kowalski, *The European Physical Journal D*, 2017, **71**, 76.

47.   R. Drozdowski, S. Werbowy, A. Kowalski and B. Pranszke, *Chemical Physics*, 2017, **483-484**, 78-83.

TABLES:

TABLE I. Collision energy dependence of the emission excitation cross sections for products of the $O^+ + Xe$ collision, given in 10^{-18} cm^2, over the 750-1000 nm optical range. Lines at 777 nm, 845 nm, and 926 nm are O emission lines and the remaining are Xe emission lines with excited state labels given in Paschen notation. A comparison of $Xe^+ + Xe$ is given for $E_{cm} = 300$ eV.

E_{cm} (eV)	777 $3p(^5P)$	845 $3p(^3P)$	926 $3d(^5D^0)$	823 $2p_6$	828 $2p_5$	835 $2p_3$	882 $2p_8$	895 $2p_6$	905 $2p_9$	916 $2p_7$	980 $2p_{10}$	992 $2p_9$
14.3	-	-	-	2.2	1.5	-	3.2	0.56	0.53	2.1	4.4	-
28.5	23.1	14.6	-	5.3	-	0.77	-	-	-	-	-	-
57.9	35.2	16.1	5.6	8.7	2.1	2.4	18.9	3.1	5.9	7.8	8.5	13.2
66.8	40	11	4	7.6	-	2.2	13.4	4.3	4.3	6.6	6.7	11.4
89.1	40.1	16.5	13.7	10.5	0.9	2.3	21.5	3.8	7.7	10.0	6.7	8.4
178.3	36.9	21.9	11.7	12.3	2.3	2.9	21.9	3.9	6.3	9.5	8.8	12.0
267.4	38.9	16.2	13.6	14.0	-	2.9	23.3	4.9	5.8	9.2	13.1	12.7
356.5	40.4	14.4	12.4	10.9	2.4	2.4	20.6	5.0	6.8	10.1	11.2	16.5
445.7	29.4	11.1	8.2	8.8	1.8	2.3	18.8	4.0	5.7	8.5	10.5	11.9
300*	-	-	-	31.2	4.97	3.67	62.0	11.2	24.8	39.0	39.6	35.1

*Cross sections of $Xe^+ + Xe$ luminescence spectra from Ref. 32.

TABLE II. Collision energy dependence of the state specific emission excitation cross sections for O_2^+ ($b, v' \rightarrow a$) and selected atomic emissions, given in 10^{-18} cm^2. Cross sections averaged over the two experimental runs for repeated collision energies. – indicates below baseline value, defined here as seven times the zero-to-max value of a range of pixels without signal.

E_{cm} (eV)	Total	$v' = 0$	$v' = 1$	$v' = 2$	$v' = 3$	$v' = 4$	Xe^+ (484 nm)	O (777 nm)	Xe (882 nm)	Baseline (7 pts)
9.8	344	149	90.5	65.8	23.4	14.8	-	-	-	0.56
19.6	382	166	106	71.0	27.6	12.1	-	-	-	0.46
39.2	349	149	103	61.3	27.0	9.5	-	-	-	0.25
58.8	404	185	114	66.0	30.0	9.0	1.06	2.46	-	0.35
118	374	180	103	57.4	23.5	9.7	1.97	4.95	1.09	0.21
235	458	232	127	62.7	31.8	4.2	3.21	6.22	1.46	0.14
470	466	235	140	55.6	35.5	0.6	1.51	6.58	1.38	0.08
941	270	134	77.9	37.3	16.6	3.6	1.62	4.22	0.91	0.07

TABLE III. Selected state specific cross sections for O_2^+ $(A, v' \rightarrow X)$ in 10^{-18} cm^2 at each collisional energy.

E_{cm} (eV)	XS	$v' = 1$	$v' = 3$	$v' = 5$	$v' = 7$	$v' = 9$	$v' = 11$	$v' = 13$	$v' = 15$	$v' = 17$	$v' = 18$
39	607	14.9	24.1	34.1	45.8	53.2	39.0	33.4	34.9	20.9	13.9
58	693	17.7	34.7	50.6	55.0	58.7	44.0	35.1	17.0	0.2	7.5
233	631	25.3	42.7	40.1	46.6	46.0	38.8	14.2	14.9	14.9	3.2

TABLE IV: Global best fit reduced LZ model results incorporating all electronic states. $d_{inner} = 3.1$ Å, $b_{max} = 5.2$ Å (left columns) and for the full MCLZ model for $d_{inner} = 3.1295$ (+0.005/-0.02) Å (four rightmost columns). Parameters are for eqn. 7. Charge-transfer cross sections (XS) given at $E_{cm} = 9.8$ eV. The meaning of the range of values under the parameters for the full MCLZ are described in the text.

Parameter	O_2^+ (b)	O_2^+ (A)	O_2^+ (a)	O_2^+ (X)	O_2^+ (b)	O_2^+ (A)	O_2^+ (a)	O_2^+ (X)
A	2.325	20$^+$	7.605	1†	4.726 (+1.4/-0.5)	2.756 (+0.8/-0.85)	0.717 (+1.03/-0.7)	4.124 (#/#)
B	1.163	1.105	1.145	0.86†	1.169 (+0.01/-0.03)	1.076 (+0.05/-0.01)	1.055 (+0.21/-0.12)	0.717 (#/#)
XS (Å^2)	8.1	28.2	21.5	0.36	3.74	9.69	2.65	~0

* *value fixed* $^+$ *value at constraint* † *values held constant* -- *did not calculate* $^\#$ *simulation not sensitive to parameter*

FIGURES:

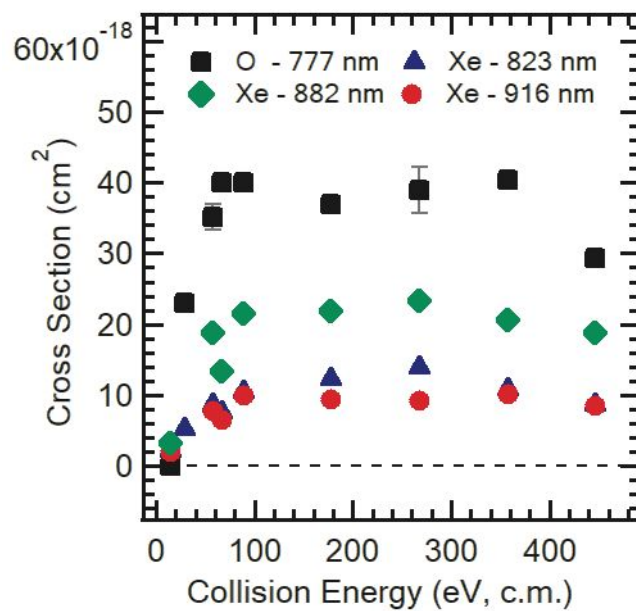**FIG.1.** Luminescence spectrum of $O^+ + Xe$ at $E_{cm} = 446$ eV. All emissions from neutral atomic species.
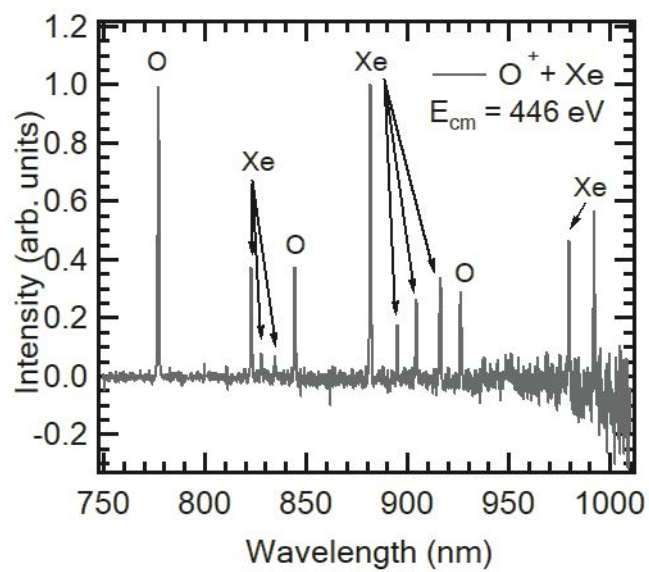
FIG. 2. Collision energy dependence of the emission excitation cross sections for selected transitions.

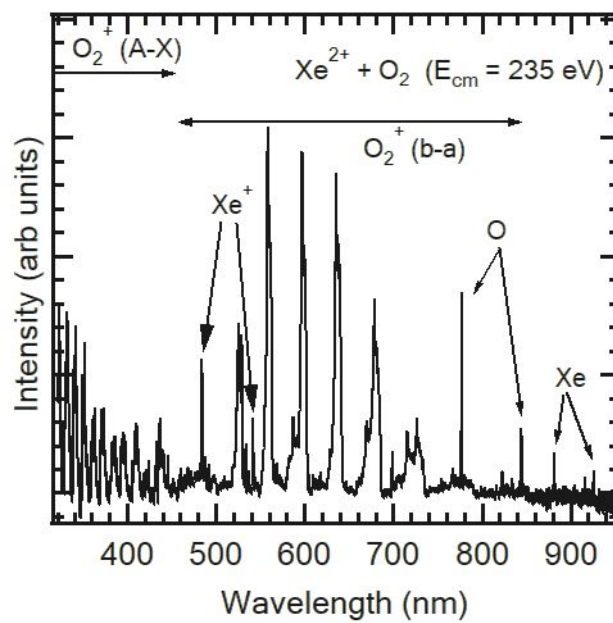**FIG.3.** Luminescence spectrum of $Xe^{2+} + O_2$ at $E_{cm} = 235$ eV with an emphasis in the (*b-a*) region.

FIG. 4. $Xe^{2+} + O_2$ at $E_{cm} = 9.8$ eV with best fit simulation overlay and resulting residual for emissions originating from O_2^+ b. An emission from atomic Xe^+ is present near 540 nm.
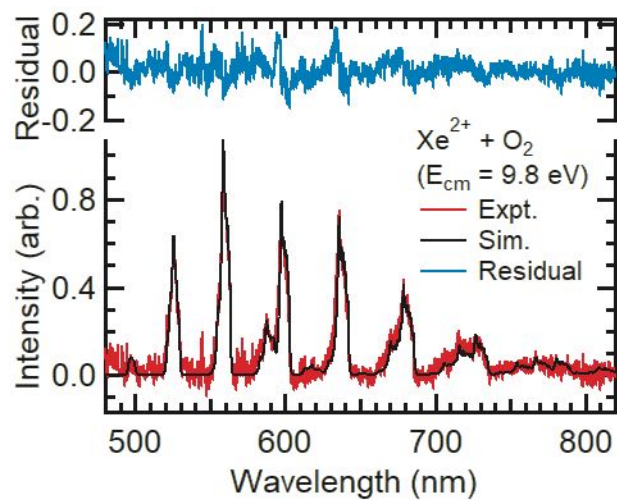
FIG. 5. Collision energy dependence of the product O_2^+ (*A-X*) and O_2^+ (*b-a*) entire band emission excitation cross sections with error bars of ± 20% for (*A-X*) (squares) and O_2^+ (*b-a*) (circles and squares). The open squares are a subset of the O_2^+ (*A-X*) band from 327.1 to 423 nm.
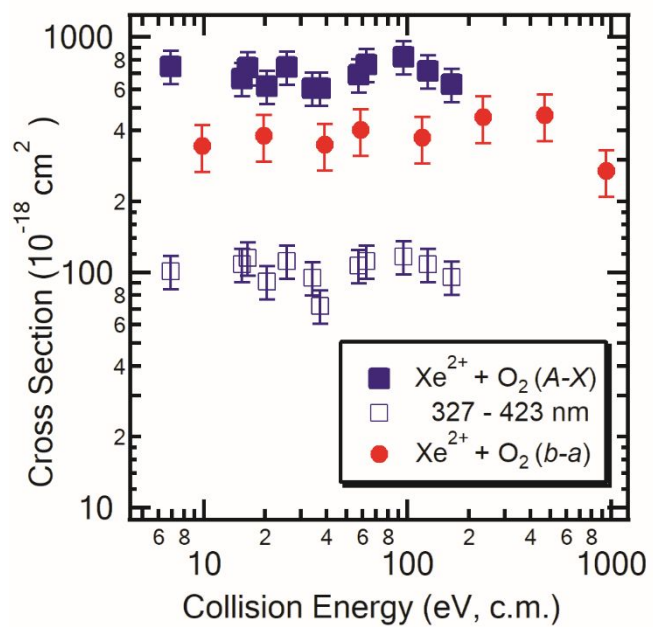
FIG. 6. O_2^+ (*b*) vibrational state populations from modeling of the O_2^+ (*b-a*) emissions (black) for the $Xe^{2+} + O_2$ collision system at select collision energies and (grey) from the Multi-Channel Landau-Zener (MCLZ) modeling with the best fit parameters. The Franck-Condon (FC) distribution assumes direct population of O_2^+ (*b*) from O_2 (*X, v = 0*). The sum of the population is normalized to unity for vibrational states from *v'= 0* to *v'=* 4 at each collision energy.
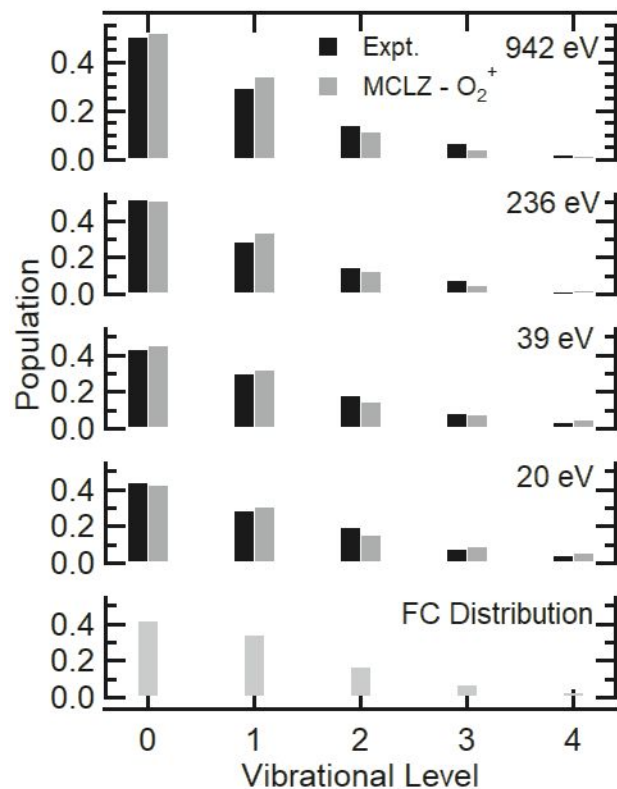
FIG. 7. Luminescence spectrum (black) of O_2^+ (A-X) resulting from collisions of $Xe^{2+} + O_2$ at $E_{cm} = 233$ eV. A best fit simulation is also given in green. The blue trace assumes a Franck-Condon distribution matching the resolution of the detection system (3.4 nm).
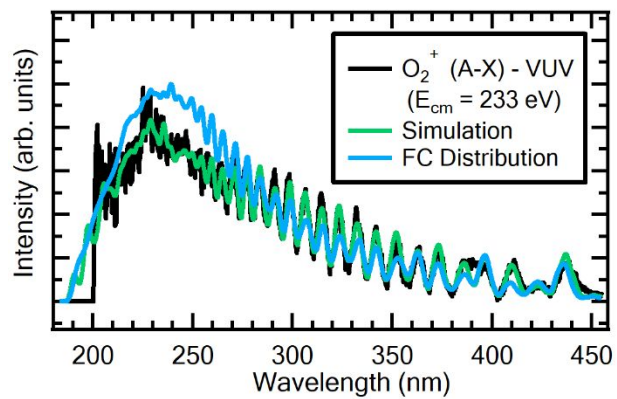
FIG. 8. O_2^+ (A) vibrational state populations derived from the vibrational analysis of the emissions measured for the Xe^{2+} + O_2 collisions at selected collision energies. The corresponding Franck-Condon distribution for ionizing O_2 (X, $v = 0$) to O_2^+ (A) is also shown. The red error bars represent the uncertainty across 10 individual simulation runs. For vibrational states from $v' = 0$ to $v' = 21$, the populations are normalized so that $\Sigma v_i = 1$.
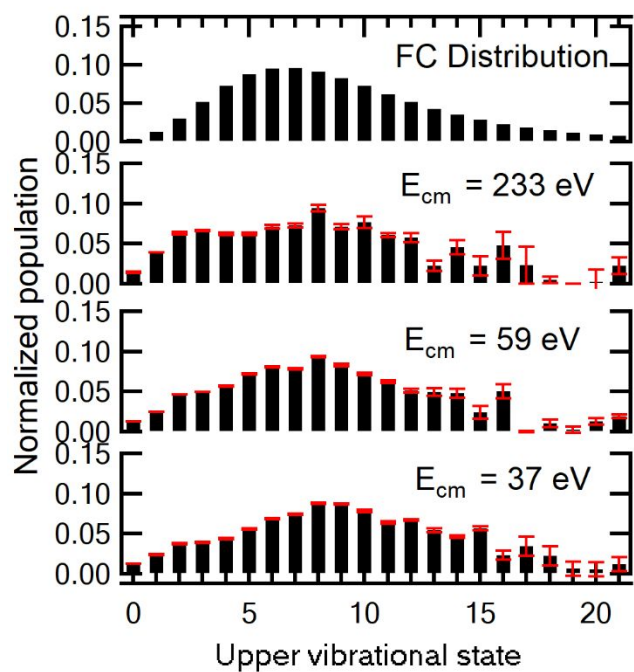
FIG. 9. *Least-square values* at $E_{cm} = 37$ eV for the a) O_2^+ (*b*) (top left) and b) O_2^+ (*A*) (top right) populations and c) O_2^+ (*b*) (bottom left) and d) O_2^+ (*A*) (bottom right) cross section values for the full MCLZ model. d_{inner} (abscissa) and the *A* parameter scaling H_{12} (ordinate) are investigated. An identical scaling factor has been applied to all four electronic states. Contours levels are 0.005 and 0.002 for a) and b). Red contours are the lowest least-square levels.
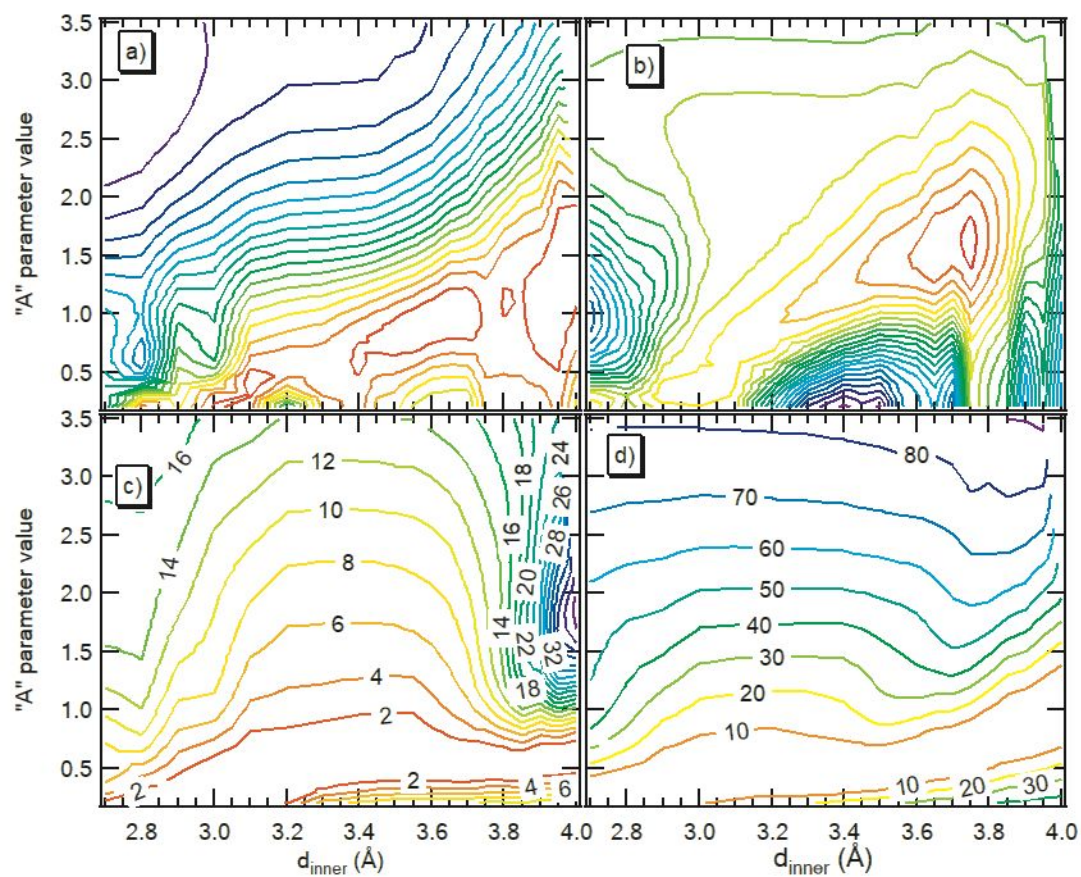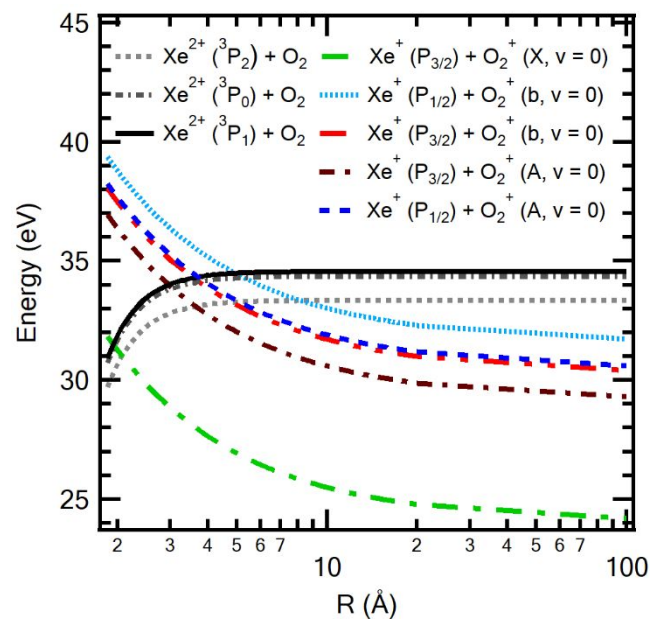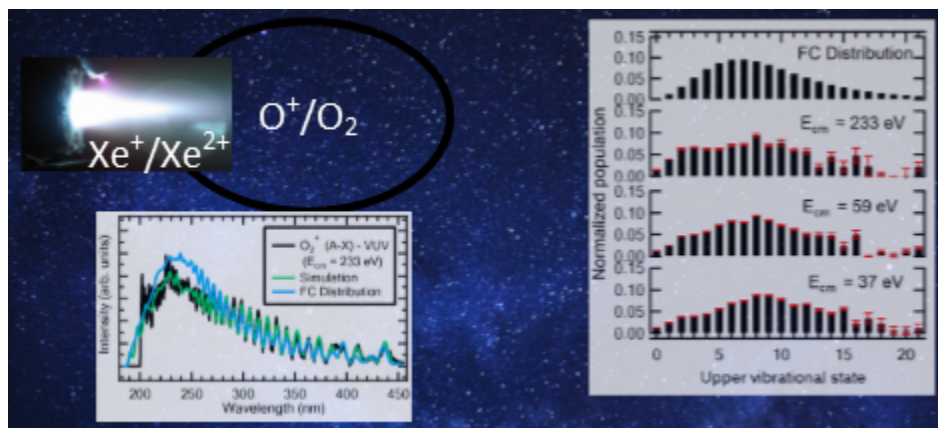
FIG. 10. Ion-induced dipole interaction potentials and product Coulombic repulsion potentials of the Xe^{2+} ($^3P_{0,1,2}$) + O_2 charge transfer system.

Vibrational state collision energy dependence of Xe/O collision systems

79x39mm (150 x 150 DPI)